AUTHOR MANUSCRIPT | PUBLICATION & REUSE INFORMATION

Design and Evaluation of a Dual-HSA Compliant Wrist Module for Prosthetic Applications

Xiaoqian Zhang, Xiyin Rong, Mario Baggetta, Cristina Piazza, and Giovanni Berselli

IEEE/ASME Transactions on Mechatronics, vol. 31, no. 4, pp. 4765-4773, 2026.

Published version: https://doi.org/10.1109/TMECH.2026.3691678

This is the author-prepared manuscript, provided on the author's personal website for individual scholarly use. Please cite the published version using the DOI above.

© 2026 IEEE. Personal use of this material is permitted. Permission from IEEE must be obtained for all other uses, in any current or future media, including reprinting/republishing this material for advertising or promotional purposes, creating new collective works, for resale or redistribution to servers or lists, or reuse of any copyrighted component of this work in other works.

Presentation preparation: publication and copyright information added. Duplicated keywords in the manuscript were corrected. The original local source file is preserved. The publisher version remains the version of record.

Design and Evaluation of a Dual-HSA Compliant Wrist Module for Prosthetic Applications

Xiaoqian Zhang, Xiyin Rong, Mario Baggetta, Cristina Piazza, and Giovanni Berselli

***Abstract*—Conventional rigid prosthetic wrists often provide limited degrees of freedom (DoFs) and poor passive adaptability under external loading. To address this limitation, this work proposes a flexible prosthetic wrist based on dual Handed Shearing Auxetic (HSA) cylinders for active flexion/extension (F/E) and pronation/supination (P/S). A wrist-oriented HSA unit design is introduced by combining a transformed lever pattern with a tailored lever angle to improve bidirectional load capability within a compact dual-cylinder architecture. A combined geometric/mechanical analysis and finite-element simulation framework is then established to investigate the influence of the main design variables on wrist functionality and performance. Based on this process, an optimized design is selected, fabricated via mold-casting, and validated experimentally using a tailored test platform integrating servo actuation, IMU sensing, and load-cell measurement. The prototype achieves approximately 49.6° F/E and 72.3° P/S motion range, about $4.1\,\mathrm{N\cdot m}$ drive torque, and over $5.8\,\mathrm{N\cdot m}$ load torque, while preserving near-linear torque–angle behavior (R^2 up to 0.99). An IMU-based PID closed-loop test demonstrates stabilization of the output-cap posture under distal loading. These results support the feasibility of HSA-based compact compliant wrist modules for prosthetic applications.**

Index Terms - Prosthetic wrist module, handed shearing auxetics (HSA), compliant mechanism, linear impedance.

I. Introduction

THE human forearm and wrist adapt flexibly to the full spectrum of everyday tasks by combining three rotational DoFs, forearm pronation–supination (P/S), wrist flexion-extension (F/E) and radial/ulnar (R/U) [1]. However, most commercially available prosthetic wrists are rigid mechanisms with a single degree of freedom [2]. Such designs fall short of replicating the human wrist's passive adaptability and compliant behavior when interacting with the environment [3], [4]. These shortcomings have been associated with wearer discomfort, unnatural compensatory movements, and fatigue during upper-limb prosthetic use and daily activities [5]–[7].

This work was supported by Horizon Europe Research and Innovation Programme INTELLIMAN (G.A. 101070136) and euROBIN (G.A. 101070596).

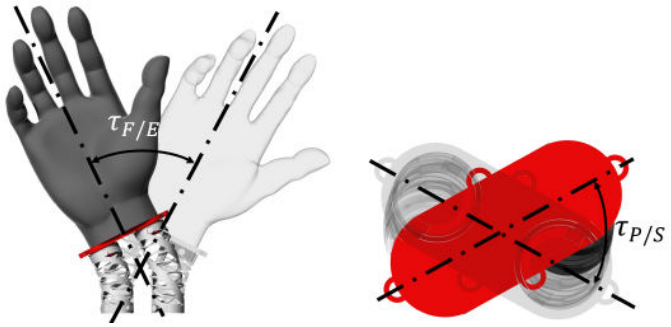
X. Zhang is affiliated with both the Department of Mechanical Engineering, University of Genoa, 16145 Genoa, Italy, and the TUM School of Computation, Information and Technology and the Munich Institute of Robotics and Machine Intelligence (MIRMI), Technical University of Munich, 80333 Munich, Germany (e-mail: xiaoqian.zhang@edu.unige.it).

X. Rong is an Independent Researcher (e-mail: xiyinrong@outlook.com).

M. Baggetta and G. Berselli are with the Department of Mechanical Engineering, University of Genoa, 16145 Genoa, Italy.

C. Piazza is with the TUM School of Computation, Information and Technology and the Munich Institute of Robotics and Machine Intelligence (MIRMI), Technical University of Munich, 80333 Munich, Germany.

Corresponding authors: Giovanni Berselli (giovanni.berselli@unige.it) and Cristina Piazza (cristina.piazza@tum.de).



(a) Motion in F/E (b) Motion in P/S

Fig. 1. Schematic representation of the proposed design: The 2-DoF wrist can move along flexion/extension (a) and pronation/supination (b).

To tackle these issues, researchers have increasingly focused on flexible wrist-joint architectures with passive compliance [8]–[10]. This inherent compliance not only boosts bionic performance [11] but also raises fault-tolerance, enabling smoother and safer interaction with the environment [3], [5], [12].

The motion direction study of the human wrist shows that the pure deviation R/U occurs much less frequently than the pure F/E or pure P/S during ADL [1]. In line with that demand, prosthetic wrists most commonly implement P/S degrees of freedom [2], because they significantly reduce trunk compensation during reaching [13]. F/E is also crucial [14]; adding an F/E wrist to an otherwise single-DoF prosthetic hand yields performance comparable to that of a high-performance multi-DoF hand without a wrist [6], and significantly reduces shoulder compensation [15]. Therefore, recent studies have integrated P/S and F/E into flexible prosthetic wrists to enhance flexibility while reducing prosthetic complexity and maintaining equivalent functionality [2], [8], [16]. Actively driven prosthetic wrists eliminate the need for passive mechanisms that rely on external forces for repositioning. This is particularly important for bilateral amputees. However, due to size and mass constraints, commercial products predominantly use a compromise solution of one active axis combined with several passive axes [2], [17].

In terms of range of motion (RoM), most ADLs can be accomplished with about 30° wrist extension, 5° wrist flexion [18], [19], 61° wrist pronation, and 75° wrist supination, well below the maximum RoM of human wrist for this DoF [20]. With respect to output torque, studies have indicated that when the driving torque reaches 2.3 Nm, amputees are generally able to participate in most ADLs and even some sports [21].

The Handed Shearing Auxetic (HSA) cylinder addresses

these targets by converting motor torque into simultaneous extension and torsion. The underlying HSA concept has been widely studied in prior work [22]. Its adjustable geometry can yield an almost linear impedance profile over large deformations, enabling finer control across different motion amplitudes, stiffness, and maximum driving torque [23], [24]. These attributes provide a promising structural basis for developing an actively driven prosthetic wrist module.

However, most existing studies still model the HSA structure as a monolithic unit [25], [26], which obscures the internal mechanisms that shape its mechanical behaviour. As a result, the exact pathways by which torque is transformed into structural deformation, and the parameters that govern tensile and compressive performance in wrist applications, remain not yet fully clarified. Yet systematic analysis of flexible prosthetic wrists that couple near-linear active motion with proportionally linear passive impedance remains limited.

This paper therefore proposes a compact, flexible prosthetic wrist with two actively powered DoFs (P/S and F/E) selected as the primary functional DoFs while achieving a balanced trade-off among size, weight, and control complexity, utilizing dual HSA cylinders (the yellow and blue parts in Fig. 2). The proposed configuration employs two identically handed HSA units, driven independently to enable wrist motions in both (P/S) ($\tau_{P/S}$ of Fig.1b) and (F/E) ($\tau_{F/E}$ of Fig.1a) directions. This arrangement provides multiple DoFs and high compliance within a compact structure. A detailed investigation has been conducted into the geometric and mechanical principles at the single-unit level, in order to clarify their influence on the overall performance of the wrist. In particular, the HSA unit was redesigned to better accommodate the bidirectional loading required by wrist operation, and finite element analysis was introduced to systematically link the main design variables to the functional and mechanical performance of the wrist. The design adopts mold-cast PU HSA cylinders and a testing platform with high structural rigidity to improve manufacturability, consistency, and measurement reliability. In addition, IMU feedback is used for closed-loop wrist control under loading conditions.

To verify this design concept, a dedicated test platform has been developed that integrates control and actuation modules (the gray parts in Fig.2 (a)). This platform has been designed to precisely measure wrist trajectories and mechanical responses under various loading and control conditions using the IMU and a load-cell based measurement system.

The rest of the paper is organized as follows: Sec. II presents the methods used for the design of the HSA unit, the robotic wrist, and the testing platform; Sec. III describes the experiments conducted to validate the proposed design; Sec. IV discusses the results obtained; and Sec. V concludes the paper.

II. Methods

A. HSA Unit

Figure 2 (b) illustrates the driving principle of the HSA structure. In essence, each HSA subunit, defined as a single cylinder cavity, unfolds into an approximate parallelogram, where torsional actuation causes vertical displacement in the Spiral Backbone (SB), varying the height of the structure. The kinematic analysis adopts a planar model, neglecting connecting rods thickness and external loads. In the default (released) state, all levers are parallel to the reference plane with length a, and the SB segment between them has length b, with spacing c. The vertical extension of each subunit is denoted by h^{cell}, and the angle between the lever and SB is θ. When twisted, the lever compresses, reducing its effective length, $a'(\theta)$, to c at the extreme limit. Conversely, in the shrink phase, the lever remains at length a, while the SBs on both sides are drawn together (ideally, they coincide). Thus, theoretically, when $\theta = 0$, the structure's outer surface consists solely of the SBs, corresponding to a minimum subunit height of $h^{\text{cell}} = h^{\min}$; when $\theta = 90°$, under this design, the subunit reaches its maximum unfolded state, corresponding to $h^{\text{cell}} = h^{\max}$. Moreover, for $\theta > 90°$, a reduction in the SB spacing leads to a dramatic compression of the central diameter d, eventually causing structural failure. Considering the effects of rod thickness and material elasticity, the actual stretch range of the HSA has been limited to between $h^{\min}$ and $h^{\max}$, with effective θ typically remaining below $90°$.

Due to the continuous flexible nature of the HSA, its kinematics have not been readily quantified by traditional rod analysis. Therefore, an area-based modeling strategy has been adopted. The unfolded HSA is considered to comprise a flexible portion, the SB, and the upper and lower caps (which serve as fixed regions). The flexible portion consists of m helical channels arranged circumferentially, each containing n subunits stacked vertically. Assuming uniform area variation during extension/compression, the unfolded area of each subunit is simplified as

$$S^{\text{cell}}(\theta) = b\, c(\theta)\, \sin\theta\, \cos\theta, \tag{1}$$

where b is the base length of a subunit and $c(\theta)$ represents the spacing between SBs as a function of θ. Thus, the total area of the flexible part is

$$S^{\text{flex}}(\theta) = m\, n\, S^{\text{cell}}(\theta). \tag{2}$$

The area of the SB, considering its thickness t^{bk} and total length $n\, b$, is given by

$$S^{\text{SB}} = t^{\text{bk}}(n\, b), \tag{3}$$

and the combined area of the upper and lower caps is denoted by S^{cap}. Hence, the total unfolded area of the HSA is

$$S^{\text{HSA}}(\theta) = S^{\text{flex}}(\theta) + S^{\text{SB}} + S^{\text{cap}} = m\, n\, S^{\text{cell}}(\theta) + t^{\text{bk}}(n\, b) + S^{\text{cap}}. \tag{4}$$

Since the base circumference of the cylindrical structure is $L = \pi d$ (with d being the diameter), the overall height is determined by

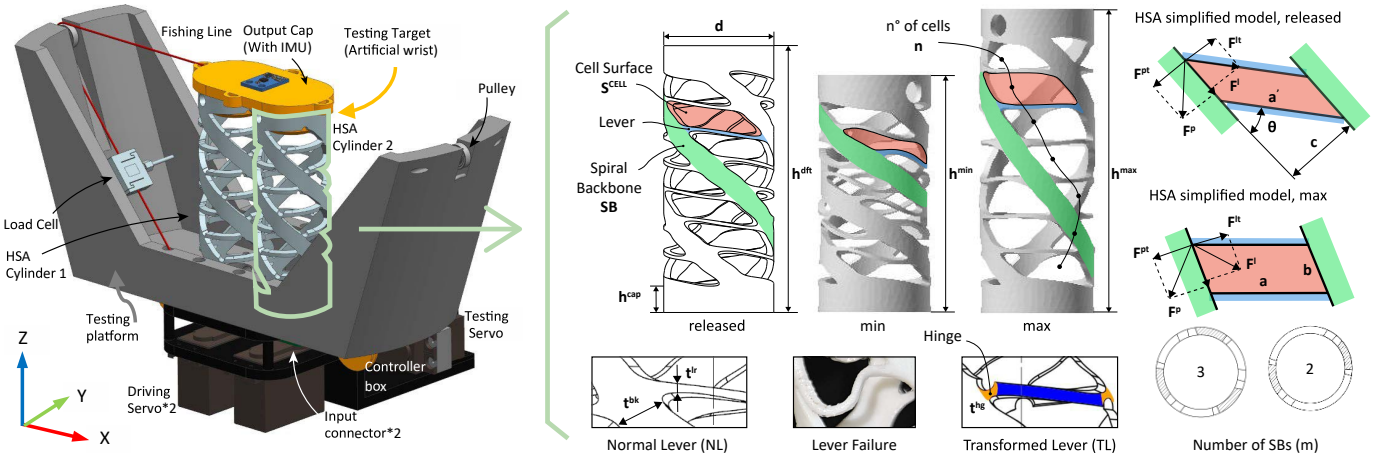
$$H(\theta) = S^{\text{HSA}}(\theta)/(\pi d). \tag{5}$$

When $S^{\text{cell}} \to 0$, the minimum height is

$$H_{\min} = (S^{\text{SB}} + S^{\text{cap}})/(\pi d), \tag{6}$$

and when the subunit is fully extended (with maximum area $S^{\text{cell}}_{\max}$, e.g., if $a'_{\max} = c_{\max}$ so that $S^{\text{cell}}_{\max} = c_{\max}\, b$), the maximum height is

$$H_{\max} = (m\, n\, S^{\text{cell}}_{\max} + S^{\text{SB}} + S^{\text{cap}})/(\pi d). \tag{7}$$



(a) Assembly of the Wrist and the Testing platform (b) Unit dimensions of the HSA Cylinder

Fig. 2. From wrist system to HSA unit: architecture, testing setup, and geometry.

Thus, the vertical stretch range (RoM) is expressed as

$$\Delta H = H_{\max} - H_{\min} = (m\, n\, S_{\max}^{\text{cell}})/(\pi d). \tag{8}$$

This model indicates that, with a fixed diameter d, increasing a (which reduces the nominal θ) and decreasing t^{bk} will lower $H_{\min}$ and expand the RoM, though an excessively high lever-to-SB width ratio may compromise stability. Overall, the model elucidates the coupled effects of design variables m, n, b, $c_{\max}$, t^{bk}, and S^{cap}.

In the mechanical analysis, the bidirectional load-bearing capability of the HSA is critical, as the performance of individual subunits collectively determines the global response. Given the uniform distribution of subunits, analyzing a single subunit suffices. Under a downward force F^p (as shown in Fig. 2 (b)), the component normal to the SB, F^{pt}, is counteracted by the lever tension F^{lt}. For a constant F^p, the relationship can be written as

$$F^{lt} = F^p \cot\theta. \tag{9}$$

Thus, for a fixed external force, the lever tension increases significantly as θ decreases. In a more general framework, the effective lever length varies with deformation according to

$$a'(\theta) = a \cdot \Phi(\theta), \tag{10}$$

$$\Phi(\theta) = \frac{c}{a} + \left(1 - \frac{c}{a}\right)\sin\theta, \tag{11}$$

where Φ is a normalized correction factor that accounts for the lever's geometric shortening as the twist angle decreases; it ranges from 1 (fully relaxed) to $\frac{c}{a}$ (fully folded). Accordingly, the lever tension can be abstractly represented as

$$F^{lt} = f(F^p, \theta, \alpha, a'(\theta)), \tag{12}$$

with α denoting the angle between the SB and the force direction. Notably, for the Normal Lever (Fig.2 (b)) that bears only tension, the inherent material and structural stiffness remain largely unaffected under compression. In contrast, if an upward force is applied (i.e., F^p is negative), the lever experiences reversed loading and may buckle, leading to nonlinear stiffness reduction. To mitigate this, the Transformed Lever configuration, featuring increased lateral thickness t^{lr} and reduced hinge thickness t^{hg} along with stiffer materials, is proposed to enhance bidirectional load capacity. The relationships between design parameters and performance metrics are summarized in Table I, together with the parameter selection for an HSA suitable for an artificial wrist. In Tab.I, performance trends are denoted by arrows: "↑" indicates that an increase in the design variable leads to an improvement (or increase) in the corresponding performance metric, while "↓" indicates the opposite. The symbols ">" and "<" are used for fixed categorical variables to denote relative performance differences. The final wrist configuration is refined through the simulation analyses described in Sec. II-D.

B. System Design

As shown in Fig. 2, the mechanical structure of the proposed artificial wrist primarily consists of two identical Handed Shearing Auxetics (HSA) cylinders ($h_c = 120\ mm$ in height, $\varphi_c = 35\ mm$ in diameter, and the gap between is $g = 1\ mm$), referred to as HSA Cylinder 1 (C1) and HSA Cylinder 2 (C2), and C1 and C2 have been fabricated by mold-casting using polyurethane (PU, Shore 90A), following the selected HSA configuration discussed previously. These cylinders have been connected to the upper Output Cap (printed from PLA) and

TABLE I
INFLUENCE OF DESIGN PARAMETERS ON HSA PERFORMANCE METRICS AND SELECTED PARAMETERS FOR THE ARTIFICIAL WRIST.

Performance Metric	a (mm)	b (mm)	n	d (mm)	t^{bk} (mm)	t^{lr} (mm)	m	NL/TL	Elastomer/Nylon
RoM	↑ ($\propto a$)	↑ ($\propto b$)	↑ ($\propto n$)	↓ ($\propto 1/d$)	↓	↓	↓	–	–
Stiffness	↓ ($\propto 1/a$)	↓ ($\propto 1/b$)	↓ ($\propto 1/n$)	–	↑ ($\propto t^{\text{bk}}$)	↑ ($\propto t^{\text{lr}}$)	↑ ($\propto m$)	NL > TL	Elastomer < Nylon
Maximum Load	↓ ($\propto 1/a$)	↓ ($\propto 1/b$)	↓ ($\propto 1/n$)	–	↑ ($\propto t^{\text{bk}}$)	↑ ($\propto t^{\text{lr}}$)	↑ ($\propto m$)	NL < TL	Elastomer < Nylon
Controllability	↓	↓	↓	–	↑	↑	↑	–	–

the MG996R metal-gear servo, which offers a rotation range of $\pm 90^{\circ}$. At 6 V input, its maximum output torque reaches 11 kg·cm.

The IMU (Adafruit_L3GD20_U) has been installed at the Output Cap such that its X-axis is aligned with the wrist's X-axis for motion tracking. Finally, an Arduino UNO microcontroller has been employed for data acquisition. By actuating the Driving Servo, the testing platform is capable of generating both P/S and F/E motions of the wrist. The IMU is used to measure the resulting trajectory and angular displacements and to provide feedback for the wrist control test described below.

C. Testing Platform

For evaluating the mechanical characteristics of the artificial wrist, a specialized testing platform has been developed (see Fig. 2), onto which the entire wrist device is mounted during experiments. The testing platform primarily consists of a fixed base, a Testing Servo, a load cell, and the control system. The Testing Servo has been configured to apply external tension on the wrist's Output Cap, while the Load Cell, mounted on a fishing line, has been employed to measure the corresponding pulling force. Figure 3 shows the control flowchart of the dedicated test rig, which contains three main tests. In the load capacity test, the test servo pulls the fishing line at a constant speed of $v_{drag} = 0.5$ mm/s while the force transducer output f is continuously recorded against the pulled distance. The test is terminated at the preset distance $s = 22$ mm (for both F/E and P/S, and in P/S both servos pull 22 mm) to generate the load–deformation curve.

In the driving ability test, the two servo horns rotate at a constant angular velocity of $v_{DRV} = 2^{\circ}\ \mathrm{s}^{-1}$ until a predetermined maximum angle 45° is reached (determined based on the simulation analysis of Section II D), and the force transducer output is continuously recorded together with the rudder rotation angle.

In the wrist control test, the servo–wrist angle mapping is used to generate the initial command for a target wrist angle, and IMU feedback is used in a closed-loop PID controller to regulate and maintain the target posture under loading conditions.

D. Actuation Mechanism and Simulation Analysis

Building on the individual HSA cylinder parameters obtained in Section II.B, Finite Element Analysis (FEA) has been conducted using ANSYS 2022R1 (Static Structural) to analyze the motion of the platform and to quantify the influence of key design variables through a design-of-experiments (DoE) study [27]. (Figure 4). The simulation model replicated the physical configuration, modeling the HSA cylinders with material properties assigned from the corresponding datasheet while all other components have been considered rigid.

Before the parametric study, a series of servo rotational angles was simulated to determine the admissible driving range of the wrist under both unloading and loading (stalled) conditions. By inspecting HSA deformation, material stress, and possible structural interferences, $\pm 70^{\circ}$ (F/E) and $\pm 80^{\circ}$ (P/S) unloading, $\pm 45^{\circ}$ (F/E and P/S) under loading, were identified as the largest controllable servo rotation without excessive stretching, compression, or collision. Under this condition, synchronous actuation of the two servos mainly generated P/S motion, whereas antagonistic actuation produced F/E motion. The maximum stress in the HSA units was approximately 7.7691 MPa, remaining below the yield strength of PU 90A.

The simulation study was then conducted in two stages. First, independent simulations were used to screen the functional suitability of the HSA unit for wrist operation by varying the lever angle θ and the lever pattern (NL/TL), and by excluding configurations in which the resulting motion deviated from the intended dominant DoF. Second, performance-oriented simulations were carried out to quantify the effects of the number of cells n, material stiffness (hardness), and two system-level variables, namely the inner radius r_{in} (equivalently, wall thickness) and the inter-cylinder distance Dist_HSA, on RoM, output torque, and stiffness-related responses. Table II

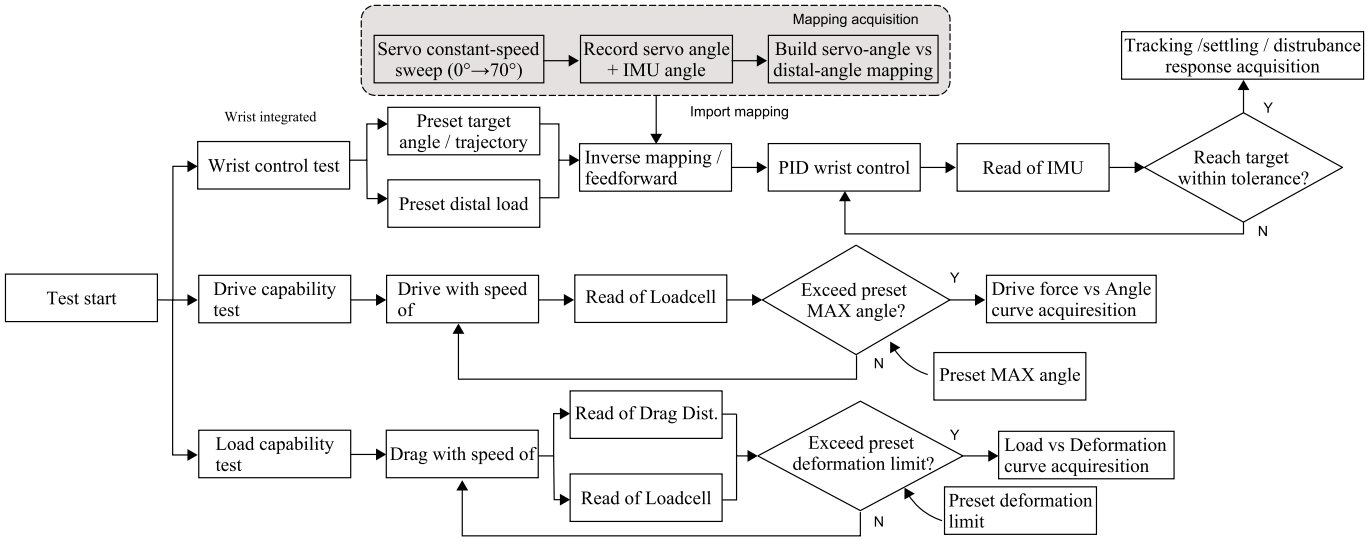


Fig. 3. Control flow chart.

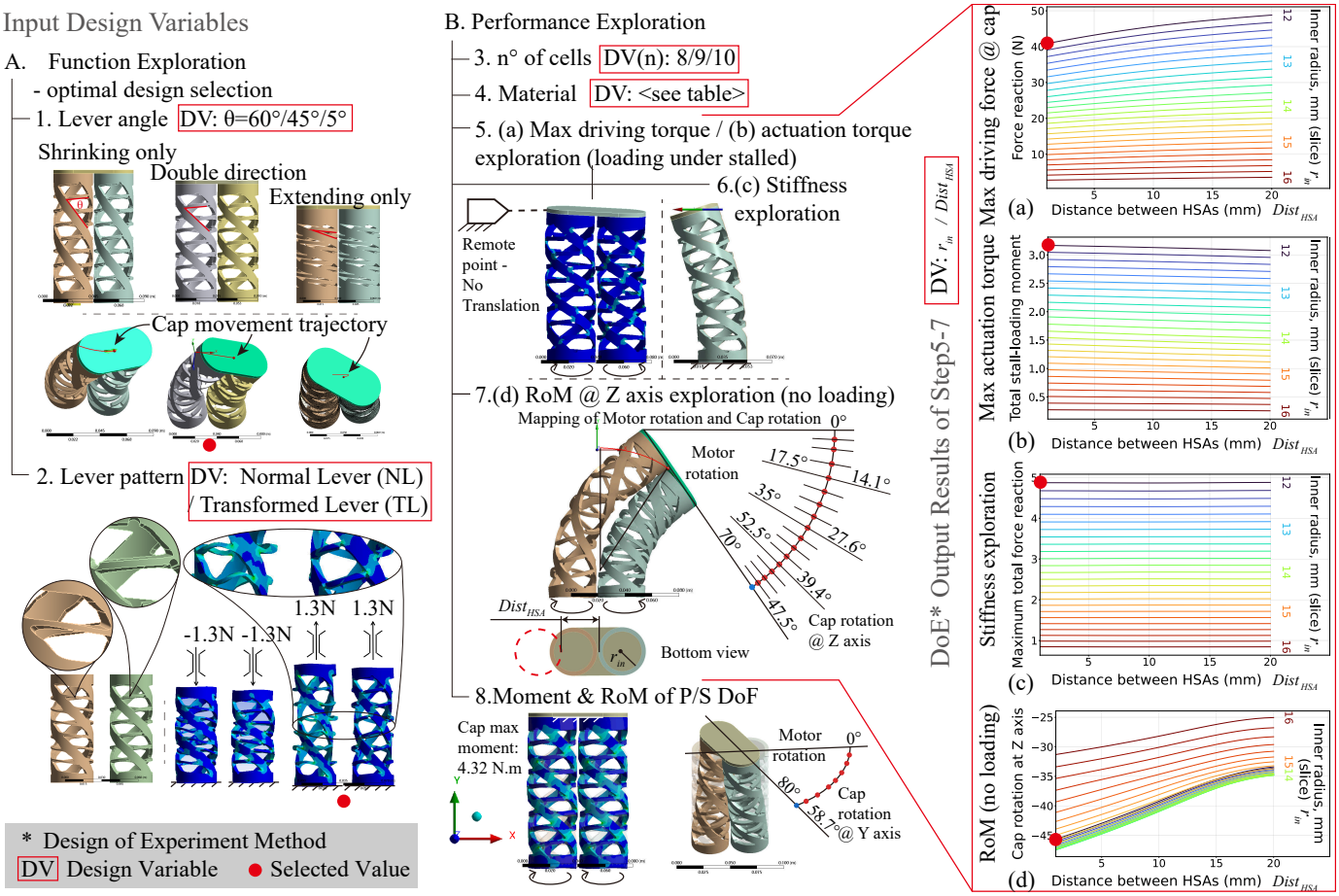


Fig. 4. Simulation setup and analysis of the HSA wrist mechanism.

TABLE II
SUMMARY OF PARAMETER SELECTION AND FINAL PERFORMANCE OF THE PROPOSED WRIST.

Group	Parameter	Selection basis / final result
Opt.	Cell number n	8: 39.4°; 9: 47.5°; 10: 54.2°. Selected: $n = 9$ (Fig. 4, Step 3).
Opt.	Material	Mold Star 40 (40A): 2.0 N·m; PU 60A: 3.2 N·m; PU 80A: 4.3 N·m; PU 90A: 4.9 N·m. Selected: PU 90A (Fig. 4, Step 4).
Fixed	Lever angle θ	Selected: 45° (Fig. 4, Step 1).
Fixed	Lever pattern	Selected: Transformed Lever (TL) (Fig. 4, Step 2).
Fixed	Inner radius r_{in}	Selected: 12 mm (Fig. 4, Steps 5–7).
Fixed	Dist_{HSA}	Selected: 1 mm (Fig. 4, Steps 5–7).

Final selected design performance: RoM about the Z axis = 45.6°; maximum driving torque = 4.1 N·m; maximum actuation torque = 3.2 N·m; stiffness exploration result = 4.9 N.

shows that material hardness and cell number were optimized comparatively, while the other parameters were fixed from the preceding simulations.

III. Experiment

The experiments have been conducted to verify the motion characteristics and mechanical performance of the artificial wrist. Since the wrist's end cap serves as the interface with the prosthetic hand, its dynamic behavior and mechanical properties directly affect the overall functional performance of the prosthesis. Therefore, both motion and mechanical responses were characterized experimentally.

A. Motion Testing

Motion tests have been conducted for both F/E and P/S movements of the wrist, including 120 actuation cycles to stabilize the HSA mechanical response. The experimental setup has followed the conditions outlined in Section II, where two HSA cylinders are driven by servos at predefined speeds and angles. Simultaneously, the IMU has been employed to record the wrist's motion. To ensure accurate angle data, the IMU has been statically calibrated at the beginning of each experiment to remove the zero offset of each axis.

After bias correction, the IMU angular velocity is discretely integrated to obtain the wrist angle:

$$\theta(t) = \theta(t - \Delta t) + [\omega(t) - \omega_{\text{bias}}] \times \Delta t, \tag{13}$$

where $\theta(t)$ is the wrist angle at time t, $\omega(t)$ is the angular velocity, ω_{bias} is the calibrated offset, and Δt is the sampling interval. The measured wrist angle was also used for PID closed-loop control.

B. Mechanical Performance Testing

In addition to the wrist-level mechanical tests, several HSA specimens with the same optimized geometry were prepared to compare the influence of material stiffness, fabrication method, and lever pattern, including mold-cast PU samples (60A, 80A, and 90A) and FDM-printed TPU samples with nominal

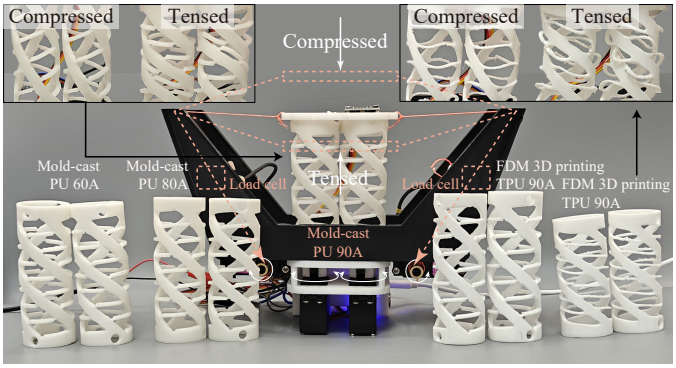


Fig. 5. Specimens and tension/compression performance test configuration used for comparing material stiffness, fabrication method, and lever pattern.

hardness of 90A. These specimens were evaluated using a dedicated tension/compression configuration (Fig. 5). Under this configuration, the HSA unit undergoes axial extension and compression rather than wrist rotation, enabling direct characterization of the bidirectional actuation capability of a single HSA unit. The reported values are measured tendon force components and are therefore expressed directly in N.

In mechanical performance tests, the driving capability and load-bearing capacity of the wrist have been examined under both F/E and P/S motions. As described in Section II, the Output Cap has been linked to a fishing line connected to a load cell and the Testing Servos. The corresponding moment arms are 0.1 m for F/E and 0.05 m for P/S.

*a) **F/E Motion: Driving Capability Test**:* The Driving Servos rotate from 0° to the maximum driving angle while the fishing line impedes the wrist's motion. The load cell measures the tension on the Output Cap during this blocking process.

*b) **F/E Motion: Load-Bearing Capacity Test**:* With the Driving Servos fixed at 0°, the fishing line is pulled by the Testing Servos until the wrist reaches its load limit. The torque is calculated by

$$\tau_{\text{F/E}} = F_{F/E} \times L_{F/E}, \tag{14}$$

where $F_{F/E}$ is the measured tension force and $L_{F/E}$ is the moment arm (0.1 m).

*c) **P/S Motion: Driving Capability Test**:* During P/S actuation, the fishing lines maintain a 90° angle with respect to the Output Cap. The torque is given by

$$\tau_{P/S} = F_{P/S} \times L_{P/S}, \tag{15}$$

where $L_{P/S} = 0.05\,\text{m}$ and $F_{P/S}$ is the measured tension.

*d) **P/S Motion: Load-Bearing Capacity Test**:* The torque is calculated as

$$\tau_{P/S} = \big(F_1 + F_2\big) \cdot \cos(\theta - 90^\circ) \times L_{P/S}, \tag{16}$$

where θ is the measured angle and $L_{P/S}$ is the moment arm. Through these methods, the tension data from the load cells are converted into torques acting on the artificial wrist.

IV. Results

Table III first reports the comparative unit-level results of the HSA specimens introduced in Sec. III. Figure 6 provides a visual representation of the artificial wrist under (F/E) and (P/S) motions.

TABLE III
Component-level comparison of HSA specimens and reference unit characteristics.

Specimen	Tension [N]	Compression [N]	Weight [g]	Notes
Specimen comparison under identical optimized geometry				
Mold-cast PU 60A	10.6	15.2	16.5	TL
Mold-cast PU 80A	26.8	33.2	16.8	TL
Mold-cast PU 90A	41.2	45.0	17.3	TL
FDM-printed TPU 90A	39.6	40.6	14.5	TL
FDM-printed TPU 90A (Normal Lever)	19.6	40.8	12.2	NL
Selected design and literature reference				
Metric	**Present PU 90A design**		**Chin et al. (2018) [28]**	
Single HSA cylinder weight	17.3 g		30.8 g	
Electromechanical system weight	148.0 g		320.2 g	
Max extended length	118 ± 1.5 mm		217 ± 7.8 mm	
Min extended length	65 ± 0.3 mm		144 ± 0.4 mm	
Stiffness (free rotation)	143.5 ± 0.2 N/m		193 ± 0.3 N/m	
Stiffness (no rotation)	262.3 ± 0.9 N/m		285 ± 0.7 N/m	
Linearity (R^2)	0.9945		N/A	

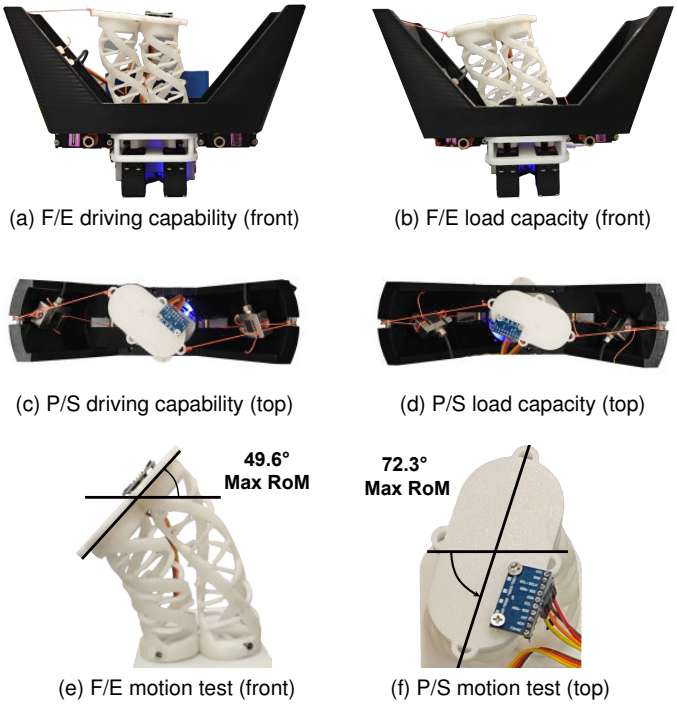


Fig. 6. States of the artificial wrist during drive and load-capacity tests. In (b) and (d) the pulling stops once the measured tension stabilises. (e)–(f) show the extreme postures reached in the motion tests.

Table III shows that, under the same optimized geometry and within the same material and fabrication category, higher material stiffness improves both tensile and compressive performance. The mold-cast PU 90A specimen outperforms the FDM-printed TPU 90A specimen, while the normal-lever

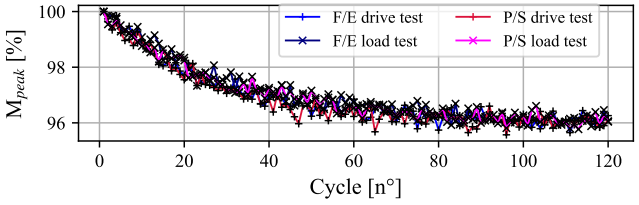
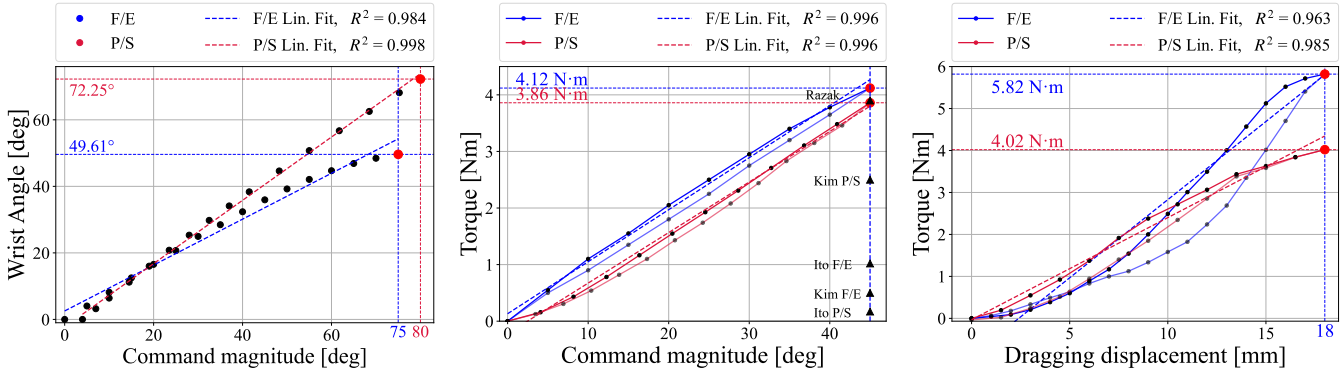
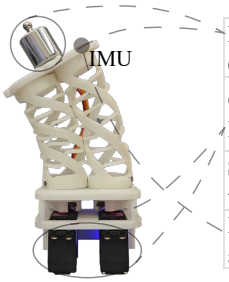


Fig. 7. Peak moments versus cycle index for F/E and P/S in drive and load tests.



(a) Servo angle vs. wrist angle (b) Drive-torque fitting (c) Load-torque curve

Fig. 8. Results of drive and load-capacity tests after mechanical stabilization. (a) Motion-test command magnitude, i.e., 0–75° for F/E and 0–80° for P/S, versus wrist output angle with linear regression. For P/S, the input denotes synchronous servo rotation $(+\theta, +\theta)$; for F/E, it denotes antagonistic rotation $(+\theta, -\theta)$. (b) Linear fit of command magnitude, 0–45°, versus driving torque for F/E and P/S, compared with [29]–[31]. (c) Fishing-line dragging displacement versus load torque for F/E and P/S.



Distal load (100g)	✓	✓	✗
Close loop PID	✓	✗	✗
Settling time	1.3 s	0.4 s	0.3 s
Measured angle	19.7°(err - 0.3°)	21.2°(err 1.2°)	20.1°(err 0.1°)

Note: Servo–wrist angle mapping was applied in all experiments. Target angle = 20° ± 0.5°.

Fig. 9. Closed-loop wrist stabilization test with a 100 g distal load: representative responses and summary table (settling time and steady-state angle error).

configuration results in a significantly reduced tensile limit. This agrees with the simulation results and supports the role of the transformed lever in improving bidirectional load capability. The lower part of the table further reports the basic dimensional and stiffness characteristics of the selected PU 90A unit and electromechanical system, together with the reference values from Chin et al. (2018) [28]. Compared with it, the present unit remains lighter and more compact, while the study further extends the comparison to material, fabrication, and lever-pattern effects.

Figure 7 presents the trend of the peak moments recorded during the drive and load tests across the first 120 operative cycles. After approximately the 100th cycle, the peak values in each test tend to stabilize. All subsequent tests have been conducted after stabilization of the material response.

Figure 8(a) compares the servo input and output-cap angles. For the two servo commands ϕ_1 and ϕ_2, the principal coordinates are defined as $u_{P/S} = (\phi_1 + \phi_2)/2$ and $u_{F/E} = (\phi_1 - \phi_2)/2$. P/S is therefore tested using synchronous/common-mode actuation $(+\theta, +\theta)$, while F/E is tested using antagonistic/differential-mode actuation $(+\theta, -\theta)$. The tested P/S and F/E commands define the principal axes of the actuation space, with intermediate command pairs corresponding to coupled P/S–F/E output-cap postures. The maximum output angle is $49.6°$ for F/E and $72.3°$ for P/S. Figure 6 illustrates the states of the artificial wrist during drive-capability and load-capacity tests in F/E and P/S motion. In Figures 6(b) and (d), the pulling action is terminated once the measured tension stabilizes, indicating that the wrist structure is near its load-bearing threshold.

Figure 8 (b) shows the drive torque versus servo input angle. At a maximum servo input of $\pm 45°$, the maximum drive torque for F/E and P/S motion has been approximately $4.1\,\mathrm{N\cdot m}$ and $3.9\,\mathrm{N\cdot m}$, respectively. Figure 8(c) shows the corresponding load-capacity results, with maximum load torques of $5.8\,\mathrm{N\cdot m}$ for F/E and $4.0\,\mathrm{N\cdot m}$ for P/S. Under the simplified single-axis test conditions, the measured moments exceed the reference torque values used for comparison. The fitted curves also show good linearity, with R^2 values in the range of 0.963–0.996.

Figure 9 reports a preliminary distal load stabilization test: under a $100\,\mathrm{g}$ load, closed-loop control reduces the steady-state angle error from about $1.2°$ to about $0.3°$, with the settling time summarized in the table.

V. Discussion and Conclusion

Through a series of experiments, this study demonstrates the initial feasibility of an artificial wrist design based on Handed Shearing Auxetics (HSA), both in terms of kinematic and mechanical performance. The results reveal a near-linear, strong correlation between servo input angles and wrist output angles, as well as a similarly linear rise in driving torque under "stalled" conditions as the servo angle increases. Not only does this indicate that a relatively simple control strategy can achieve precise posture regulation, but it also partially mimics the human wrist's biological response whereby "larger deformations correspond to greater resistance." To further support this, the influence of the geometric parameters of individual HSA subunits on the global structural behavior has been analyzed, and a mathematical model describing these dependencies has been derived. Based on this analysis, an HSA unit configuration for wrist use has been identified and fabricated, and its stiffness and deformation range have been experimentally validated. While the current design covers the targeted functional range for typical ADLs in both F/E and P/S, further efforts will focus on validation under dynamic, multi-directional external loads and on improving robustness in more

realistic use scenarios. On the other hand, the experiments also reveal certain limitations. Two distinct methods have been used to measure maximum torque: a) holding the wrist at its default position and simply pulling its distal end, and b) obstructing its movement with a fishing line during servo actuation. While these approaches effectively quantify the wrist's extreme motion and load capacities, real-world usage commonly involves scenarios where the wrist alternates or combines active driving and passive deformation under dynamic, multi-directional external loads. It has been observed that single-condition tests cannot fully encapsulate how this structure performs in more complex operations (e.g., grasping objects of various shapes, bimanual coordination, or high-frequency interactions). Therefore, although our study confirms linear mechanical properties and coverage of typical ADL torque and RoM requirements, understanding the device's performance under diverse dynamic conditions remains an ongoing task.

Given these findings, future work will focus on dynamic load capacity and closed-loop stabilization under coupled, multi-DoF deformations. In addition, the repeatability of the mold-casting process will be quantified across multiple specimens to further improve confidence in manufacturability and experimental consistency. In conclusion, this research has provided quantitative evidence supporting the feasibility of adopting an HSA-based structure for a compliant 2-DoF wrist module. The device has achieved significant motion ranges, near-linear responses in the two principal actuation modes, and increasing impedance in tandem with greater deformations. With further verification under realistic distal loads, off-axis disturbances, and coupled multi-DoF operation, this design has the potential to be adapted to prosthetic systems requiring richer forms of interaction.

REFERENCES

[1] W. Anderton, S. Tew, S. Ferguson, J. Hernandez, and S. K. Charles, "Movement preferences of the wrist and forearm during activities of daily living," *Journal of Hand Therapy*, vol. 36, no. 3, pp. 580–592, 2023.

[2] N. M. Bajaj, A. M. Dollar, and A. J. Spiers, "State of the art in artificial wrists: A review of prosthetic and robotic wrist design," *IEEE Transactions on Robotics*, vol. 35, no. 1, pp. 261–277, 2019.

[3] P. Capsi-Morales, C. Piazza, G. Grioli, A. Bicchi, and M. G. Catalano, "A three degrees of freedom switchable impedance myoelectric prosthetic wrist," *The International Journal of Robotics Research*, vol. 43, no. 11, pp. 1649–1675, 2024.

[4] G. Kanitz, F. Montagnani, M. Controzzi, and C. Cipriani, "Compliant prosthetic wrists entail more natural use than stiff wrists during reaching, not (necessarily) during manipulation," *IEEE Transactions on Neural Systems and Rehabilitation Engineering*, vol. 26, no. 7, pp. 1407–1413, 2018.

[5] M. Deijs, R. M. Bongers, N. D. M. Ringeling-van Leusen, and C. K. van der Sluis, "Flexible and static wrist units in upper limb prosthesis users: Functionality scores, user satisfaction and compensatory movements," *Journal of NeuroEngineering and Rehabilitation*, vol. 13, no. 1, p. 26, 2016.

[6] F. Montagnani, M. Controzzi, and C. Cipriani, "Is it finger or wrist dexterity that is missing in current hand prostheses?" *IEEE Transactions on Neural Systems and Rehabilitation Engineering*, vol. 23, no. 4, pp. 600–609, 2015.

[7] Ø. Stavdahl, "Optimal wrist prosthesis kinematics: Three-dimensional rotation statistics and parameter estimation," Ph.D. dissertation, NTNU: Norwegian University of Science and Technology, 2002.

[8] A. Demofonti *et al.*, "Design of a modular and compliant wrist module for upper limb prosthetics," *The Anatomical Record*, vol. 306, 2022.

[9] G. Lee, G. Y. Hong, and Y. Choi, "Tendon-driven compliant prosthetic wrist consisting of three rows based on the concept of tensegrity structure," *IEEE Robotics and Automation Letters*, vol. 6, no. 2, pp. 3956–3963, 2021.

[10] S. Casini *et al.*, "Design of an under-actuated wrist based on adaptive synergies," in *2017 IEEE International Conference on Robotics and Automation (ICRA)*, 2017, pp. 6679–6686.

[11] J. Zhou, H. Cao, W. Chen *et al.*, "Bioinspired soft wrist based on multicable jamming with hybrid motion and stiffness control for dexterous manipulation," *IEEE/ASME Transactions on Mechatronics*, vol. 28, no. 3, pp. 1256–1267, 2023.

[12] M. Baggetta, G. Palli, C. Melchiorri, and G. Berselli, "A monolithic cable-driven compliant wrist for prosthetic arms," *IEEE/ASME Transactions on Mechatronics*, vol. 29, no. 2, pp. 1052–1063, 2024.

[13] A. J. Metzger, A. W. Dromerick, R. J. Holley, and P. S. Lum, "Characterization of compensatory trunk movements during prosthetic upper limb reaching tasks," *Archives of Physical Medicine and Rehabilitation*, vol. 93, no. 11, pp. 2029–2034, 2012.

[14] N. Moser, M. K. O'Malley, and A. Erwin, "Importance of wrist movement direction in performing activities of daily living efficiently," in *2020 42nd Annual International Conference of the IEEE Engineering in Medicine & Biology Society (EMBC)*, 2020, pp. 3174–3177.

[15] T. Bertels, T. Schmalz, and E. Ludwigs, "Objectifying the functional advantages of prosthetic wrist flexion," *JPO: Journal of Prosthetics and Orthotics*, vol. 21, no. 2, pp. 74–78, 2009.

[16] T. Lenzi, J. Lipsey, and J. W. Sensinger, "The RIC arm—a small anthropomorphic transhumeral prosthesis," *IEEE/ASME Transactions on Mechatronics*, vol. 21, no. 6, pp. 2660–2671, 2016.

[17] H. H. Sears, E. Iversen, S. Archer, J. Linder, and J. R. MacDonald, "Evaluation studies of new electric terminal devices," in *Myoelectric Symposium*, 2005.

[18] A. K. Palmer, F. W. Werner, D. Murphy, and R. Glisson, "Functional wrist motion: A biomechanical study," *The Journal of Hand Surgery*, vol. 10, no. 1, pp. 39–46, 1985.

[19] D. L. Nelson, M. A. Mitchell, P. G. Groszewski *et al.*, "Wrist range of motion in activities of daily living," in *Advances in the Biomechanics of the Hand and Wrist*. Springer, 1994, pp. 329–334.

[20] R. Damerla *et al.*, "Design and testing of a novel, high-performance two dof prosthetic wrist," *IEEE Transactions on Medical Robotics and Bionics*, vol. 4, no. 2, pp. 502–519, 2022.

[21] H. Fan, G. Wei, and L. Ren, "Prosthetic and robotic wrists comparing with the intelligently evolved human wrist: A review," *Robotica*, vol. 40, no. 11, pp. 4169–4191, 2022.

[22] R. L. Truby *et al.*, "Soft somatic robots with handed shearing auxetics," *Science*, vol. 359, no. 6371, pp. 155–159, 2018.

[23] R. L. Truby, L. Chin, and D. Rus, "A recipe for electrically-driven soft robots via 3d printed handed shearing auxetics," *IEEE Robotics and Automation Letters*, vol. 6, no. 2, pp. 795–802, 2021.

[24] I. Good, T. Brown-Moore, A. Patil *et al.*, "Expanding the design space for electrically-driven soft robots through handed shearing auxetics," in *2022 International Conference on Robotics and Automation (ICRA)*, 2022, pp. 10 951–10 957.

[25] A. Garg *et al.*, "Kinematic modeling of handed shearing auxetics via piecewise constant curvature," in *2022 IEEE 5th International Conference on Soft Robotics (RoboSoft)*, 2022, pp. 423–430.

[26] M. Stölzle *et al.*, "Modelling handed shearing auxetics: Selective piecewise constant strain kinematics and dynamic simulation," in *2023 IEEE International Conference on Soft Robotics (RoboSoft)*, 2023, pp. 1–8.

[27] S. M. Kargar, A. Parmiggiani, M. Baggetta, E. Ottonello, G. Hao, and G. Berselli, "Optimization of a tetrahedron compliant spherical joint via computer-aided engineering tools," *The International Journal of Advanced Manufacturing Technology*, vol. 132, no. 3, pp. 1151–1162, 2024.

[28] L. Chin, J. Lipton, R. MacCurdy *et al.*, "Compliant electric actuators based on handed shearing auxetics," in *2018 IEEE International Conference on Soft Robotics (RoboSoft)*, 2018, pp. 100–107.

[29] K. Ito *et al.*, "An emg controlled prosthetic forearm in three degrees of freedom using ultrasonic motors," in *Proceedings of the Annual International Conference of the IEEE Engineering in Medicine and Biology Society*, 1992, pp. 1487–1488.

[30] Y.-J. Kim *et al.*, "Roboray hand: A highly backdrivable robotic hand with sensorless contact force measurements," in *2014 IEEE International Conference on Robotics and Automation (ICRA)*, 2014, pp. 6712–6718.

[31] N. Abd Razak, N. Abu Osman, H. Gholizadeh, and S. Ali, "Development and performance of a new prosthesis system using ultrasonic sensor for wrist movements: A preliminary study," *BioMedical Engineering OnLine*, vol. 13, no. 1, p. 49, 2014.

VI. Biography Section



Xiaoqian Zhang Xiaoqian Zhang received the M.Eng. degree in Industrial Design Engineering from Guangdong University of Technology, China, in 2019. He is currently a doctoral candidate in Mechanical Engineering jointly supervised between the University of Genoa, Italy, and the Technical University of Munich, Germany. Before joining his doctoral program, he was a full-time Research Assistant at the Shenzhen Institutes of Advanced Technology, Chinese Academy of Sciences. His current research focuses on the mechanisms and control development of the soft and compliant robotic prosthetics, and grippers.



Xiyin Rong Xiyin Rong received the M.E. degree in Industrial Engineering from Tiangong University, China, in 2018. Her background includes mechanical design, CAD-based modelling, mechatronic system development, and engineering data analysis. She has industrial experience in semiconductor equipment development and non-standard mechanical design, including equipment modification, parameter optimization, troubleshooting, and 3D modelling for mechanical components. Her research interests include mechanical design, mechatronic systems, data-supported engineering analysis, and assistive robotic devices.



Mario Baggetta received his M.Sc., and Ph.D. degrees in Mechanical Engineering from the University of Genova in 2019, and 2023, respectively. Following his doctoral studies, he held postdoctoral positions at the University of Bologna and the University of Naples "Federico II". Currently, he is an Assistant Professor at the Department of Mechanical, Energy, Management and Transportation Engineering, University of Genova. His research interests include the integrated design of compliant mechanisms, variable stiffness actuators, cable-driven systems, and robotic hands for manipulation and prosthetics. He is actively involved in several research projects, including the FISA 2023 COMPANION project on compliant components for robotic manipulation and the HE IntelliMan project, which aims to develop an AI-based manipulation system for advanced robotic services and prosthetics.



Cristina Piazza Cristina Piazza received a B.Sc. in Biomedical Engineering, a M.S. in Automation and Robotics Engineering and a PhD degree in Robotics (summa cum laude, 2019) from the University of Pisa (Italy). She subsequently moved to Chicago (USA) where she worked as a postdoctoral researcher at Northwestern University. Since 2020, Prof. Piazza is tenure track assistant professor at Technical University of Munich. She is IEEE Senior Member and has received numerous awards for her scientific work, including the IEEE/RAS Early Career Award (2026), and the Kevin P. Granata Award (2026). Her main research interests include the study of human movement and the design of artificial devices based on soft robotics technologies for robotic and prosthetic applications.



Giovanni Berselli is Full Professor and Chair of Design Methods for Industrial Engineering at the University of Genova, Italy, where he coordinates the PhD Degree in Mechanical, Energy and Management Engineering. He is also Affiliated Researcher with the Advanced Robotics Department at the Italian Institute of Technology (IIT). Prof. Berselli is IEEE Senior Member, a Fellow of the ASME, the Chair of ASME – Italy Section, and the past Chair of the ASME Technical Committee on Modeling, Dynamics, and Control of Adaptive Systems. He has held Excellence Fellowships at TUM, DLR, KIT and visiting professor poistion and Harvard, MIT, MGH, UTwente and University of Navarra. Prof. Berselli's scientific activity is focused on the design, modelling and experimental evaluation of: i) robot hands and grippers; ii) compliant mechanisms and soft actuators for safe human-robot interaction; iii) energy-aware industrial robotics.